Structural and Morphological Properties of WO_3 Nanoparticles Synthesized Under Varying Laser Fluences

Iman Abdul Salam[1, a)], Adawiya J. Haider[1, b)], Azhar I. Hassan[1, c)], Chafic Salame[2, d)] and Ali J. Addie[2, e)]

[1]*Applied Sciences Department, Laser Science and Technology Branch, University of Technology, Baghdad, Iraq.*
[2]*European Academy for Sustainable Development, EURACA, 11, rue du Rempart Saint Thiébault, 57 000, METZ, France.*
[3]*Center of Industrial Applications and Materials Technology, Scientific Research Commission, Baghdad, Iraq.*

[a)]*eman19921991@gmail.com*
[b)] *Corresponding authors: adawiya.j.haider@uotechnology.edu.iq*
[c)] *azhar.i.hassan@uotechnology.edu.iq*
[d)] *salame@euraca.fr*
[e)] *ali.jaddie@yahoo.com*

Abstract: Tungsten oxide (WO_3) nanoparticles were synthesized via pulsed laser ablation in liquid (PLAL) under varying laser fluences to investigate the correlation between ablation energy and nanoscale structural evolution. The study demonstrates that precise tuning of laser energy enables control over crystallinity, morphology, and optical response through plasma–liquid interactions. X-ray diffraction confirmed the monoclinic WO_3 phase, with crystallite size decreasing from ~47 nm at 100 mJ to ~28 nm at 350 mJ due to enhanced fragmentation and rapid quenching. FESEM and TEM analyses revealed a morphological transition from well-dispersed spherical nanoparticles at low fluence to fused, irregular aggregates at high fluence. EDS spectra verified the high purity of the synthesized material, with slight oxygen enrichment typical of PLAL-derived oxides. UV–Vis absorbance spectra indicated a strong dependence on fluence, with the 100 mJ sample exhibiting the highest optical activity and sharpest band-edge transition, attributed to quantum confinement and reduced defect density. These findings establish an optimal fluence window (100–150 mJ) for producing uniform, crystalline, and optically active WO_3 nanoparticles. The work validates PLAL as a scalable, green, and tunable approach for designing high-performance semiconductor nanostructures for photocatalytic and optoelectronic applications.

Keywords: Tungsten oxide (WO_3); Pulsed laser ablation in liquid (PLAL); Nanostructure engineering; Photocatalytic nanomaterials; Laser fluence; Optical properties.

INTRODUCTION

The increasing global demand for sustainable environmental technologies has driven rapid advancements in photocatalysis, a solar-driven process that utilizes semiconductor materials to generate redox reactions for pollutant degradation and renewable fuel production [1–5]. Among various metal oxide semiconductors, tungsten oxide (WO_3) has attracted significant attention due to its moderate bandgap (2.4–2.8 eV), enabling efficient absorption of the blue region of the solar spectrum [6–9]. As a transition metal oxide, WO_3 combines chemical robustness, strong optical activity, and high photostability, making it a promising material for applications in photoelectrochemical cells, gas sensors, electrochromic devices, and environmental photocatalysis. The photocatalytic mechanism of semiconductor materials, illustrated in Fig. 1, involves the generation of photoinduced charge carriers upon light irradiation with energy equal to or greater than the bandgap ($h\nu \geq Eg$). This process promotes electrons from the valence band (VB) to the conduction band (CB), leaving behind positively charged holes in the VB. The spatial separation of these carriers drives redox reactions at the semiconductor–liquid interface: photogenerated electrons reduce adsorbed O_2 molecules to superoxide radicals ($O_2^{-}\bullet$), while holes oxidize surface hydroxyl groups or water molecules to form hydroxyl radicals ($\bullet OH$) [10, 11]. Among various metal oxides, tungsten oxide (WO_3) has attracted significant attention owing to its chemical stability, suitable bandgap (2.4–2.8 eV), and strong visible-light absorption. Structurally, WO_3 exists in several polymorphic forms, including tetragonal (α-WO_3, >740 °C), orthorhombic (β-WO_3, 330–740 °C), monoclinic I (γ-WO_3, 17–330 °C), triclinic (σ-WO_3, −43–178 °C), and monoclinic II (ε-WO_3, <−43 °C) [12]. At room temperature, monoclinic γ-WO_3 is the most stable phase. Despite its favorable optical response, pristine WO_3 typically exhibits limited photocatalytic efficiency due to its relatively low conduction-band edge potential, which hinders the reduction of O_2 and accelerates electron–hole recombination under visible-light excitation [13–15]. Recent research

has focused on overcoming the intrinsic photocatalytic limitations of WO_3 through nanoscale engineering strategies aimed at enhancing charge carrier separation, surface reactivity, and band structure alignment [8, 16, 17]. Nanostructured WO_3 has been synthesized using various conventional techniques such as hydrothermal, solvothermal, and microwave-assisted routes. Although effective, these chemical-based methods often involve multiple processing steps, toxic reagents, and limited control over particle purity and stoichiometry, reducing their environmental and industrial compatibility [16, 18, 19]. In contrast, pulsed laser ablation in liquid (PLAL) has emerged as a green, versatile, and single-step alternative for producing high-purity nanomaterials with tunable morphology and composition [5, 20, 21]. During PLAL, the interaction of high-energy laser pulses with a solid target immersed in a liquid medium generates a plasma plume that undergoes rapid cooling and condensation to form stable colloidal nanoparticles. The resulting particle characteristics are governed by key laser parameters, such as fluence, wavelength, pulse duration, and repetition rate, which collectively influence plasma dynamics, nucleation, and subsequent growth kinetics [5, 22, 23]. This study investigates how laser fluence influences the structural, morphological, and optical properties of WO_3 nanoparticles synthesized via PLAL. We hypothesize that varying laser energy modulates plasma–liquid thermodynamics, thereby controlling crystallinity, defect density, and particle size, factors critical to photocatalytic performance. By correlating laser parameters with microstructural and optical responses, the work aims to define an optimal fluence window that balances crystallinity and surface reactivity. The results establish PLAL as a sustainable and tunable route for producing high-purity WO_3 nanostructures for environmental and energy applications.

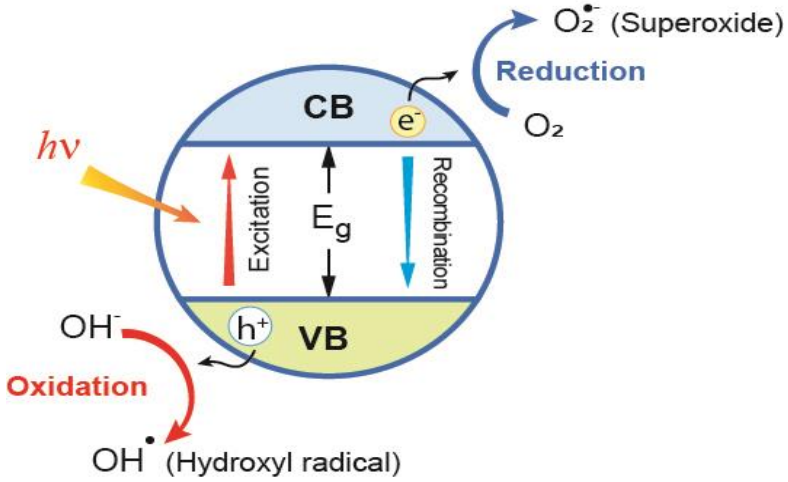

FIGURE 1. Schematic illustration of the photocatalytic mechanism in a semiconductor under visible-light excitation, showing charge generation, separation, and surface redox reactions.

MATERIAL AND METHOD

WO_3 powder was pressed into a pellet using a 6-ton hydraulic press to yield disks of 2 cm diameter and approximately 3 mm thickness, To fabricate the laser ablation target. After that, the pellets were sintered for an hour at 1100°C to improve their mechanical integrity. Deionized water was employed in all experimental procedures. The production of WO_3 nanoparticles was accomplished by pulsed laser ablation in liquid. With λ = 532 nm and 100 pulses, a Q-switched Nd:YAG laser was focused at the WO_3 pellet submerged in deionized water. The ablation was conducted at three different laser energies: 100,150, and 350 mJ. Fig. 2 shows the schematic overview of the synthesis route, which includes a process based on heat and laser.

The crystalline phase and structural order of the samples were ascertained by X-ray diffraction (XRD) examination using a Shimadzu XRD-6000 diffractometer running with Cu Kα radiation (λ = 1.5406 Å) at a scan rate of 3°/min. The crystallite size was calculated by X-ray line broadening analysis using the Scherrer equation. Field emission scanning electron microscopy (FESEM) was used to examine the surface morphology and elemental composition using a ZEISS Sigma device that was outfitted with energy-dispersive X-ray spectroscopy (EDS). To reduce agglomeration, all measurements were taken at 25 °C after the colloidal solutions had been sonicated for ten minutes.

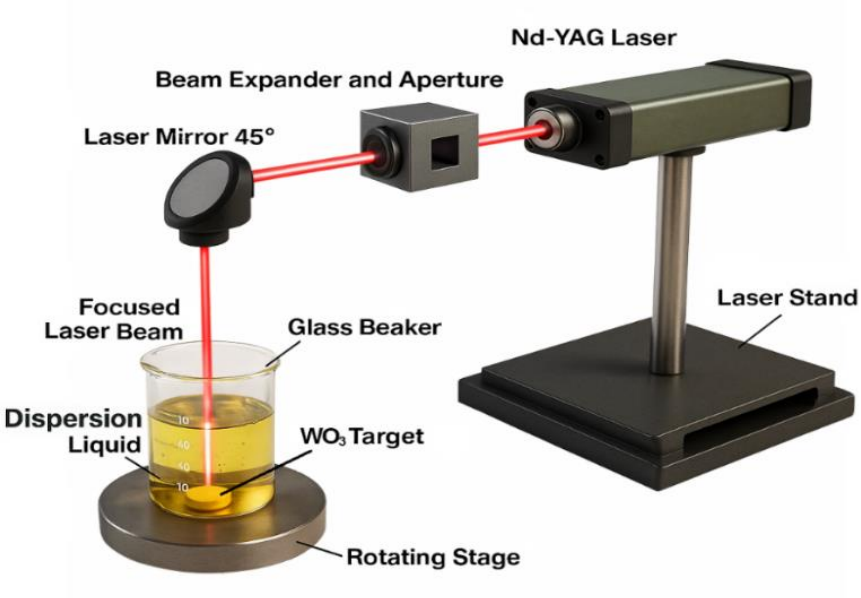

FIGURE 2: Schematic representation of the synthesis route for WO_3 nanoparticles by pulsed laser ablation in liquid (PLAL), including target sintering and laser–liquid interaction processes.

RESULTS AND DISCUSSION

The XRD patterns in Fig. 3 confirm that all WO_3 nanoparticle samples formed via PLAL at 100, 150, and 350 mJ energies are of the monoclinic tungsten oxide phase (WO_3). The observed diffraction peaks at $2\theta \approx 23.1°$, 23.6°, and 24.4° correspond to the (002), (020), and (200) lattice planes, respectively, matching established WO_3 reference patterns (e.g. JCPDS #43-1035) and prior PLAL-derived WO_3 studies [19, 24]. Additional weaker peaks at (112), (022), (220), (004), and (400) further support phase purity without detectable secondary phases or tungsten suboxides. As laser fluence increases, the peak widths evolve systematically. At 100 mJ the peaks are broad but distinct, indicating moderate crystallite size and defect content. At 150 mJ, further broadening and intensity reduction suggest a reduction in coherent domain size and increased lattice disorder, likely due to more intense plasma-liquid interactions and faster quenching. At 350 mJ, the peaks partially sharpen again, signaling a partial recovery of crystallinity, plausibly via localized heating and annealing within the transient plasma environment.

Using the Scherrer relation [25, 26], the estimated crystallite sizes decrease from ~47 nm at 100 mJ to ~32 nm at 150 mJ, and further to ~28 nm at 350 mJ. This monotonic decline implicates increased ablation energy as a driver for higher nucleation rate, stronger fragmentation, and more abrupt cooling, factors that suppress crystal growth and favor smaller grains. The partial recovery of peak sharpness at 350 mJ may reflect a competition between high-temperature reordering and rapid solidification that constrains the maximum crystallite growth.

From a theoretical standpoint, the crystallite size evolution is governed by plasma plume dynamics and its interaction with the surrounding liquid medium. At higher pulse energies, denser and hotter plumes generate intense shock waves, cavitation, and turbulence that fragment nascent nuclei and promote rapid quenching, leading to smaller crystallites [27]. At lower fluence, the plume expansion is less violent, allowing nuclei to coalesce and grow for longer durations before solidification. The partial recrystallization observed at 350 mJ indicates a threshold where transient heating enables limited atomic diffusion and structural reordering before quenching.

Comparable behavior has been reported for WO_3 nanoparticles synthesized via PLAL across different fluence regimes, where crystallinity and bandgap show non-linear correlations with energy input due to plasma–liquid coupling and cumulative heat effects [28]. Across laser-synthesized oxide systems, similar fluence dependence has been observed, moderate fluences yield optimal particle quality, whereas excessive energy promotes fragmentation and structural disorder [29].

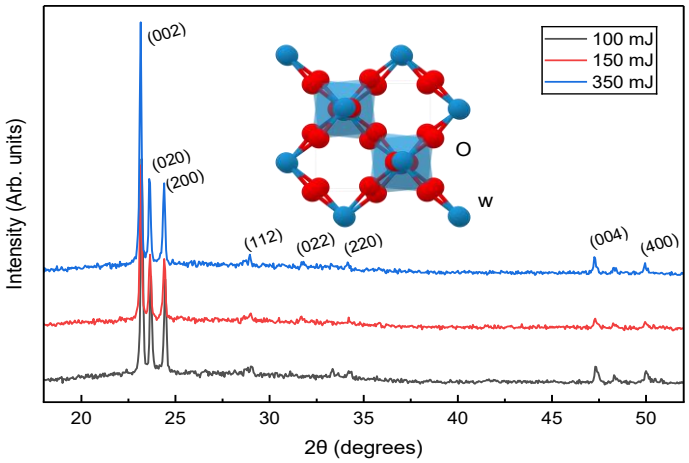

FIGURE 1. XRD patterns of WO_3 nanoparticles synthesized by PLAL at 100, 150, and 350 mJ, showing monoclinic WO_3 phase with main peaks at (002), (020), and (200). The inset illustrates the WO_3 crystal structure and fluence-dependent changes in crystallinity.

The present findings therefore align with these reports: increasing fluence enhances nucleation and fragmentation, reducing crystallite size, while excessive heating can locally restore order through short-range diffusion. This interplay defines an optimal fluence window for tailoring WO_3 nanostructures with balanced crystallinity and defect density, crucial for achieving high photocatalytic activity through improved surface reactivity and charge transport.

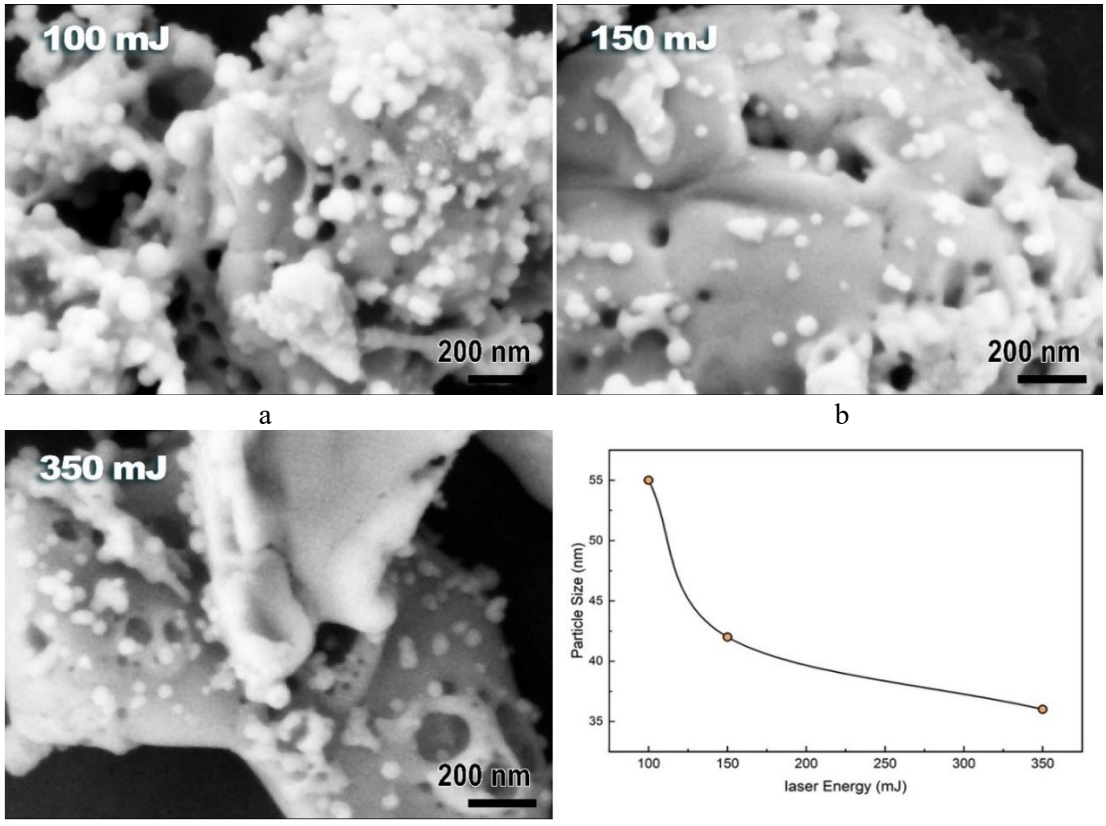

FIGURE 2a,b,c,d. FESEM micrographs of WO_3 nanoparticles synthesized by PLAL at 100, 150, and 350 mJ, showing fluence-dependent morphological evolution from dense agglomerates to finer, porous structures. The inset plot illustrates the decrease in average particle size with increasing laser energy.

Figure 4 shows the FESEM micrographs of WO_3 nanoparticles synthesized by pulsed laser ablation in liquid (PLAL) at laser energies of 100, 150, and 350 mJ, along with the corresponding particle size trend. The morphological evolution reflects the strong dependence of ablation dynamics on laser fluence. At 100 mJ, the surface exhibits dense agglomerates composed of nearly spherical nanoparticles with diameters of 50–55 nm, indicative of limited ablation efficiency and moderate thermal input. Increasing the fluence to 150 mJ results in a more porous and heterogeneous morphology, where particles appear smaller (~40 nm) and more uniformly distributed, suggesting enhanced fragmentation and re-nucleation under intensified plasma–liquid interactions. At 350 mJ, the nanostructure becomes more irregular, with partially melted surfaces and aggregated clusters (~35 nm average size), consistent with strong thermal gradients and rapid quenching effects within the cavitation zone. The particle size decreases monotonically with increasing laser fluence, as illustrated in the inset, following the trend derived from XRD analysis. This reduction arises from the enhanced ablation rate and stronger plasma-induced shock waves at higher fluence, which increase nucleation density and limit particle coalescence [27, 30]. The observed morphological transition from compact agglomerates to finer, porous, and irregular structures aligns with reported PLAL behavior in other metal oxide systems, where excessive fluence promotes surface melting and rapid resolidification [27, 31, 32]. The combined XRD and FESEM observations confirm that higher laser energy enhances both fragmentation and re-nucleation kinetics, producing smaller and more crystalline WO_3 nanoparticles, which are advantageous for photocatalytic and optoelectronic applications.

Figure 5 displays the EDS spectra of WO_3 nanoparticles synthesized via pulsed laser ablation in liquid (PLAL) at laser energies of 100, 150, and 350 mJ, along with the corresponding quantitative composition. All spectra confirm the presence of tungsten (W) and oxygen (O) as the only constituent elements, verifying the successful formation of WO_3 without detectable impurities. The strong O–Kα peak near 0.5 keV and the characteristic W–M and W–L emission lines between 1.7–2.3 keV and 8–11 keV, respectively, appear consistently across all samples, indicating compositional stability and reproducibility. The absence of additional peaks confirms the chemical purity of the nanoparticles and reflects one of the key advantages of the PLAL process, its ability to produce stoichiometrically clean oxides directly from pure solid targets without chemical precursors [27]. Quantitative analysis (table in Figure 5d) reveals a slight oxygen excess relative to the ideal WO_3 stoichiometry, with O/W atomic ratios of ~5.0–5.2. This mild oxygen enrichment is characteristic of PLAL-synthesized oxides and can be attributed to post-ablation oxidation of the molten clusters in water and the possible formation of WO_3 or higher oxide phases [30]. The variation in laser fluence shows negligible influence on the overall O/W ratio, suggesting that oxygen incorporation is governed primarily by plasma–liquid chemical equilibrium rather than ablation energy. Such oxygen-rich compositions are beneficial for photocatalytic activity, as surface hydroxylation and oxygen vacancies can enhance charge separation and reaction kinetics [6]. These findings corroborate the XRD and FESEM results, confirming that PLAL produces phase-pure, compositionally stable WO_3 nanoparticles with tunable structural order and high chemical purity.

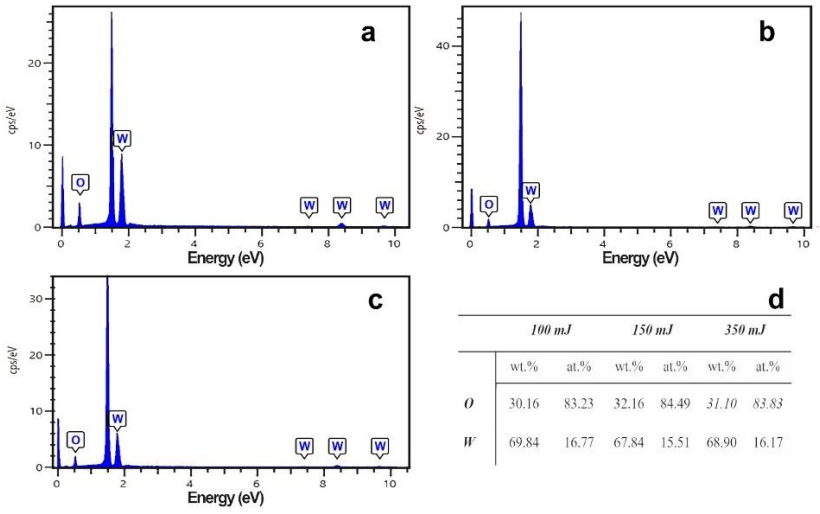

	100 mJ		150 mJ		350 mJ	
	wt.%	at.%	wt.%	at.%	wt.%	at.%
O	30.16	83.23	32.16	84.49	*31.10*	*83.83*
W	69.84	16.77	67.84	15.51	68.90	16.17

FIGURE 5. EDS spectra of WO_3 nanoparticles synthesized by PLAL at (a) 100 mJ, (b) 150 mJ, and (c) 350 mJ, showing only tungsten and oxygen peaks with no detectable impurities. (d) Quantitative elemental analysis indicates consistent O/W ratios and slight oxygen enrichment across laser fluences.

Figure 6 shows the UV–Vis absorbance spectra of WO_3 nanoparticles synthesized by pulsed laser ablation in liquid (PLAL) at laser energies of 100, 150, and 350 mJ. All samples exhibit strong absorption in the ultraviolet region (200–400 nm), characteristic of electronic transitions from the O 2p valence band to the W 5d conduction band in semiconducting WO_3. The main absorption edge is observed between 256–260 nm, consistent with the fundamental band-to-band excitation of monoclinic WO_3. The gradual decrease in absorbance toward longer wavelengths (400–600 nm) reflects tail states within the bandgap, commonly associated with oxygen vacancies, lattice disorder, or hydrated surface layers.

The sample prepared at 100 mJ displays the highest optical absorbance and a sharper absorption edge, indicating enhanced light-harvesting efficiency and a narrower defect distribution. This behavior can be attributed to smaller and more uniform nanoparticles, as confirmed by XRD and FESEM analyses, which showed finer crystallites (~47 nm) and a more homogeneous morphology. The improved absorption is consistent with the quantum confinement effect, where reduced particle dimensions increase the transition probability and slightly widen the optical bandgap [33]. In contrast, the spectra at 150 mJ and 350 mJ exhibit a red-shifted and less intense absorption, reflecting partial aggregation and increased structural disorder due to excessive plasma heating and re-solidification effects during high-fluence ablation. Such behavior parallels observations reported for PLAL-synthesized WO_3 and TiO_2 systems, where higher fluence induces defect-mediated sub-band states that broaden the Urbach tail and suppress excitonic absorption [34, 35].

The correlation between optical and structural properties highlights the interdependence of plasma dynamics and electronic structure. At lower fluence, moderate plasma temperatures favor stoichiometric WO_3 with minimal defect density, while excessive energy input leads to over-ionization, rapid quenching, and oxygen-rich amorphous surface layers that reduce band-to-band absorption. This interpretation aligns with the EDS results showing slight oxygen enrichment and with theoretical models predicting that localized oxygen states near the conduction band can act as recombination centers, thereby lowering optical activity [36]. The enhanced absorbance at 100 mJ confirms that moderate fluence provides an optimal balance between crystallinity, particle size, and stoichiometry. These conditions yield WO_3 nanoparticles with superior optical properties desirable for photocatalysis, photoelectrochemical water splitting, and UV photodetection applications.

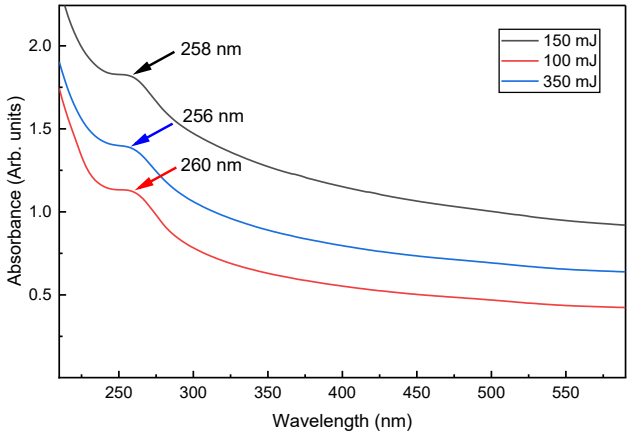

FIGURE 6. UV–visible absorption spectra of WO_3 nanoparticles synthesized at laser energies of 100, 150, and 350 mJ, illustrating optical band-edge behavior and fluence-dependent absorbance.

Figure 7 presents the TEM micrographs of WO_3 nanoparticles synthesized by PLAL at laser energies of 100, 150, and 350 mJ using a 532 nm Nd:YAG laser (1 Hz, 100 pulses). The microstructural evolution reflects the strong influence of laser fluence on plasma–liquid dynamics, particle nucleation, and subsequent growth behavior.

At 100 mJ (Figure 7a), the nanoparticles exhibit a uniform, nearly spherical morphology with average diameters ranging from 15 to 30 nm. The particles are moderately aggregated but retain well-defined boundaries, suggesting that the moderate plasma temperature at this fluence favors homogeneous nucleation and rapid quenching, suppressing extensive coalescence. The resulting fine and uniform particles correspond well with the high optical absorbance and sharper band-edge transition observed in the UV–Vis spectra (Figure 6), confirming the correlation between nanoscale size and enhanced quantum confinement effects [33].

Increasing the fluence to 150 mJ produces larger, partially fused nanoparticles (30–60 nm) with irregular boundaries and porous agglomerates. The stronger laser–target interaction at this energy elevates plasma temperature and ejection rates, increasing the probability of particle collision and coalescence during condensation. This effect

parallels the crystallite-size reduction detected by XRD (Figure 2), which results from simultaneous fragmentation and re-nucleation processes under dynamic ablation–re-solidification conditions [27].

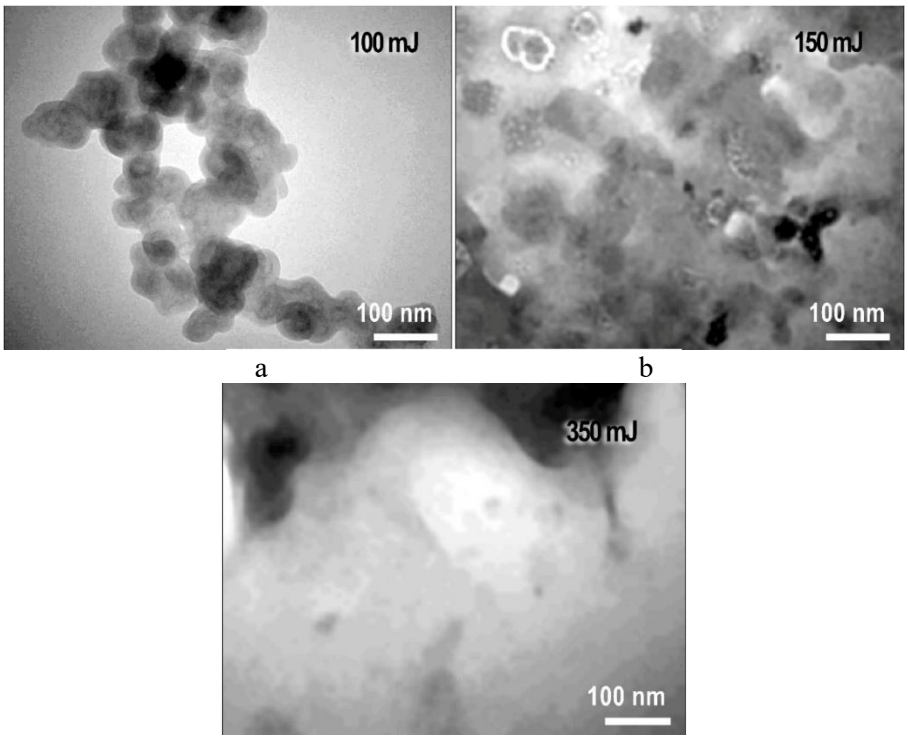

FIGURE 7a,b,c. Transmission electron microscopy (TEM) images of WO_3 nanoparticles obtained at 100, 150, and 350 mJ, highlighting particle size evolution, aggregation tendency, and crystallite morphology.

At 350 mJ, the morphology transforms into dense, fused clusters with average dimensions exceeding 70 nm, accompanied by significant loss of particle uniformity. The excessive plasma heating at this fluence induces localized melting and re-crystallization, producing compact aggregates with reduced surface area. Similar fluence-dependent aggregation and grain coarsening behavior have been reported for PLAL-synthesized WO_3 and TiO_2 systems, where over-energized plasma plumes promote rapid particle growth and sintering in the confined liquid medium [37].

The TEM findings are thus consistent with the structural and optical analyses: lower fluence (100 mJ) favors uniform, nanosized WO_3 particles with enhanced crystallinity and optical activity, whereas higher fluence leads to thermal coalescence, reduced homogeneity, and lower optical performance. The observed morphology evolution underscores the delicate balance between ablation energy, plasma thermodynamics, and cooling rate that governs particle nucleation and growth in PLAL-synthesized metal oxides.

CONCLUSION

This study systematically elucidates the influence of laser fluence on the structural, morphological, and optical properties of WO_3 nanoparticles synthesized via pulsed laser ablation in liquid (PLAL). The results demonstrate that fine control over laser energy effectively tailors crystallinity, particle size, and optical response through modulation of plasma–liquid interactions and cooling kinetics. XRD analysis revealed the formation of monoclinic WO_3, with crystallite size decreasing from ~47 nm at 100 mJ to ~28 nm at 350 mJ, highlighting a fluence-dependent balance between fragmentation and recrystallization dynamics. FESEM and TEM observations confirmed that increasing fluence induces a transition from discrete, uniformly dispersed nanoparticles to dense, coalesced aggregates, driven by enhanced plasma temperature and localized melting. EDS analysis verified the chemical purity of the synthesized WO_3, with only W and O detected, and a consistent oxygen enrichment typical of PLAL-derived oxides. UV–Vis spectra further established that the 100 mJ sample exhibited the highest optical absorbance and sharpest band-edge, signifying optimized nanoscale confinement and minimal defect density. Conversely, higher fluence caused reduced absorbance due to excessive heating and structural disorder.

Collectively, these findings establish 100–150 mJ as the optimal fluence window for producing uniform, crystalline, and optically active WO_3 nanoparticles. The results validate PLAL as a scalable, green, and tunable synthesis platform capable of engineering defect-controlled nanostructures for advanced photocatalytic and optoelectronic applications. The insights into plasma-driven nucleation and growth mechanisms presented here provide a foundation for precision design of metal oxide nanomaterials using environmentally benign laser-based fabrication routes

ACKNOWLEDGMENTS

The authors acknowledge the College of Applied Science, University of Technology–Iraq, and the Center of Industrial Applications and Materials Technology, Scientific Research Commission, Baghdad, Iraq, for technical support. The constructive discussions and collaborative environment provided by colleagues within the Scientific Research Commission greatly contributed to the success of this work..

REFERENCES

1. D. Vaya, B. Kaushik, and P. K. Surolia, Mater. Sci. Semicond. Process. 137, 106181 (2022).
2. S. Bhowmik et al., Inorg. Chem. Commun. 182, 115577 (2025).
3. Y. Liu, S. Sun, M. Ma, H. Pan, F. Gao, and X. Huang, J. Environ. Chem. Eng. 12, 114986 (2024).
4. N. A. A. Mohd Amin and H. F. Mohd Zaid, Int. J. Hydrogen Energy 77, 166–183 (2024).
5. A. H. Attallah, F. S. Abdulwahid, Y. A. Ali, and A. J. Haider, Plasmonics 19, 2581–2594 (2024).
6. M. G. Peleyeju and E. L. Viljoen, J. Water Process Eng. 40, (2021).
7. Y. Liu, R. Wang, Y. Zhao, and H. Wang, Inorg. Chem. Commun. 182, 115431 (2025).
8. J. Sidawi et al., Microelectron. Int. 31, 90 (2014).
9. F. A. Fadhil, F. I. Sultan, A. J. Haider, and R. A. Rsool, AIP Conf. Proc. 020056 (2019).
10. X. Sun et al., Angew. Chem. Int. Ed. 61, (2022).
11. M. S. Mathew et al., Nanomaterials 13, 12 (2023).
12. P. A. Shinde and S. C. Jun, ChemSusChem 13, 11–38 (2020).
13. X. Song et al., Crystals 11, (2021).
14. S. Tosoni, C. Di Valentin, and G. Pacchioni, J. Phys. Chem. C 118, 3000–3006 (2014).
15. M. Palivos et al., AIP Conf. Proc. 1968, 030076 (2018).
16. O. M. Pinto et al., Processes 12, (2024).
17. E. Boateng, S. S. Thind, S. Chen, and A. Chen, Electrochem. Sci. Adv. 2, (2022).
18. J. Zhu et al., J. Phys. Chem. C 114, 16335–16342 (2010).
19. E. T. Salim, A. I. Hassan, F. A. Mohamed, M. A. Fakhri, and A. J. Addie, J. Mater. Sci. Mater. Electron. 34, 1546 (2023).
20. A. Addie, K. S. Khashaan, J. Saimon, and A. Hassan, Iraqi J. Sci. 62, 2197–2203 (2021).
21. S. M. Talib, A. J. Haider, S. Al-Musawi, F. S. Al-Joudi, and S. A. Ahmed, Plasmonics **** (2025).
22. S. I. Hussein et al., Opt. Mater. 155, 115890 (2024).
23. F. S. Abdulwahid, A. J. Haider, and S. Al-Musawi, AIP Conf. Proc. 020039 (2023).
24. E. T. Salim, A. I. Hassan, F. A. Mohamed, and M. A. Fakhri, J. Opt. 53, 3749–3769 (2024).
25. A. J. Addie, S. S. Batros, and A. I. Hassan, Thin Solid Films 818, 140669 (2025).
26. A. M. Yahya, A. I. Hassan, E. T. Salim, and A. J. Addie, J. Alloys Compd. 1001, 175133 (2024).
27. R. C. Forsythe, C. P. Cox, M. K. Wilsey, and A. M. Müller, Chem. Rev. 121, 7568–7637 (2021).
28. F. Barreca, N. Acacia, S. Spadaro, G. Currò, and F. Neri, Mater. Chem. Phys. 127, 197–202 (2011).
29. B. G. Moura et al., Opt. Laser Technol. 97, 20–28 (2017).
30. V. Amendola et al., Chem. Eur. J. 26, 9206–9242 (2020).
31. A. P. Sreekala et al., Beilstein J. Nanotechnol. 16, 1428–1498 (2025).
32. N. al-huda A. Abass, M. F. Jawad, and A. J. Haider, Lasers Manuf. Mater. Process. 11, 931–945 (2024).
33. M. R. Waller et al., Chem. Mater. 24, 698–704 (2012).
34. J. C. Murillo-Sierra et al., Chem. Eng. J. Adv. 5, 100070 (2021).
35. S. Lettieri et al., Materials 14, 1645 (2021).
36. M. B. Johansson et al., J. Phys. Chem. C 121, 7412–7420 (2017).
37. J. Theerthagiri et al., Light Sci. Appl. 11, 250 (2022).